Optics Letters

Quantum-inspired detection for spectral domain optical coherence tomography

SYLWIA M. KOLENDERSKA,[1,2,*] FRÉDÉRIQUE VANHOLSBEECK,[1,2] AND PIOTR KOLENDERSKI[3]

[1] The Dodd-Walls Centre for Photonic and Quantum Technologies, New Zealand
[2] The Department of Physics, The University of Auckland, Auckland 1010, New Zealand
[3] Faculty of Physics, Astronomy and Informatics, Nicolaus Copernicus University, Grudziądzka 5, 87-100 Toruń, Poland
*Corresponding author: skol745@aucklanduni.ac.nz

Received 20 March 2020; revised 13 May 2020; accepted 15 May 2020; posted 15 May 2020 (Doc. ID 393162); published 18 June 2020

Intensity levels allowed by safety standards (ICNIRP or ANSI) limit the amount of light that can be used in a clinical setting to image highly scattering or absorptive tissues with optical coherence tomography (OCT). To achieve high-sensitivity imaging at low intensity levels, we adapt a detection scheme—which is used in quantum optics for providing information about spectral correlations of photons—into a standard spectral domain OCT system. This detection scheme is based on the concept of dispersive Fourier transformation, where a fiber introduces a wavelength-dependent time delay measured by a single-pixel detector, usually a high-speed photoreceiver. Here, we use a fast superconducting single-photon detector SSPD as a single-pixel detector and obtain images of a glass stack and a slice of onion at the intensity levels of the order of 10 pW. We also provide a formula for a depth-dependent sensitivity falloff in such a detection scheme, which can be treated as a temporal equivalent of diffraction-grating-based spectrometers.

https://doi.org/10.1364/OL.393162

Optical coherence tomography (OCT) is a fast, noncontact, and noninvasive technique enabling high-resolution 3D imaging [1]. In almost three decades since its inception, OCT has become widespread in various areas of biology and medicine with continual expansion in clinical applications for diagnostic and intraoperative purposes [2]. The quality of OCT images is practically limited by the ability of the detection unit to efficiently acquire light backscattered from an object. In a clinical setting, the photon budget becomes even smaller, because the intensity levels of light illuminating the imaged tissue must lie within ANSI standards or ICNIRP guidelines. For example, for eyes, the safety level is of the order of 1.7 mW and 5 mW at wavelengths around 800 nm and 1060 nm, respectively, as calculated for 10 s of continuous wave exposure [3]. In some situations, the permissible light power densities do not allow high-fidelity imaging, especially when the object under investigation is highly scattering or absorptive.

The approach of mapping a spectrum of an optical pulse to a temporal waveform by means of a long fiber spool and a single-pixel detector is called dispersive Fourier transformation (DFT) [4]. It has already been used in OCT to time-stretch light from a supercontinuum source [5] and Ti:sapphire laser [6] at the input of the interferometer and perform swept-source-like OCT at axial scan rates of up to 90 MHz.

Here, we propose a spectral detection scheme, which is increasingly used in quantum optics to study spectral correlations of photons [7]. It is based on the principles of dispersive Fourier transformation—a fiber spool induces wavelength-dependent time delay, and a single-pixel detector, which in this case is a single-photon detector, provides a fast and ultrasensitive time acquisition. We show that such combination allows OCT imaging at light power levels, which are at least 5 orders of magnitude lower than the safety standards. We report basic characteristics of such a detection system at 1550 nm and present images of a glass stack and an onion showing that the quality is comparable to the images obtained with standard OCT systems with similar axial resolution and imaging range characteristics.

The OCT system with the quantum-inspired spectral detection is presented in Fig. 1. Pulsed light with a central wavelength of 1550 nm and a total spectral bandwidth of 115 nm [MenloSystems T-Light, spectrum depicted in Fig. 2(a)] is inputted into a Linnik–Michelson interferometer through a fiber collimator FB1 ($f = 11$ mm). The repetition rate of the laser, 100 MHz, allows for a temporal broadening of up to 10 ns before adjacent pulses start to overlap each other. In the detection part, we decided to use a 5-km-long fiber spool (SMF28E, Fibrain) with a group velocity dispersion, β_2, equal to 23 fs^2/mm, which broadened the pulses coming from the interferometer to 9.6 ns. The output port of the fiber spool was monitored by a superconducting single-photon detector (SSPD) (Scontel) whose detection range is 350–2300 nm and with a peak quantum efficiency approximately 65% at 1550 nm [8]. The SSPD outputs an electric pulse after each successful detection of a single photon, and the field-programmable gate array (FPGA) electronics measure the timestamps of the electric pulses. The timing jitter of the apparatus consisting of the SSPD and the time tagging unit is 35 ps, which is very close to the state of the art, but an order of magnitude worse than for a standard photodiode. This detector does not resolve photon numbers. Due to the high sensitivity of the SSPD, the light source was attenuated to a level of single photons per pulse by

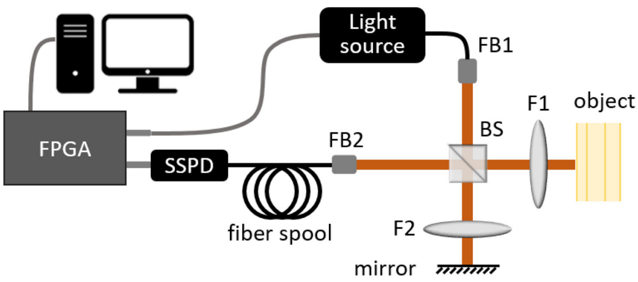

Fig. 1. Experimental setup. The light source is a pulsed laser attenuated to a level of single photon per pulse. Pulses are coupled to a fiber (FB1) and propagate in a Linnik–Michelson interferometer. The input wave packet (pulse) is then split at a beam splitter (BS) into two arms. In the object arm, one wave packet interacts with the object and acquires an additional phase; in the reference arm, the other one is reflected from the mirror. They both overlap at the beam splitter, and the output is coupled to a single-mode fiber spool using a fiber coupler FB2. The time-resolving superconducting single-photon detector (SSPD) together with the long dispersive fiber spool work as a spectrometer. Time reference is provided by a photodiode signal from the light source. The data are collected using an FPGA time-stamping electronics. F1 and F2, lenses.

using a half-wave plate and a polarization beam splitter at the input of the interferometer. The SSPD was synchronized with the fast built-in photodiode in the light source. Because the fiber spool—through the phenomenon of dispersion—delays each wavelength by a different amount of time, time measurement performed by the SSPD provided a spectrum of the light at the input of the fiber collimator FB2 ($f = 11$ mm). Measured spectra were digitized by FPGA electronics and were saved onto a computer. Because the fiber spool's dispersion curve is not a linear function in wavenumber, a linearization of the acquired spectra was performed [9].

The integration time of a single spectrum was set to 1 s and allowed us to measure timestamps of photons in several consecutive pulses. With a bin size of 10 ps and a time window of 10 ns, the spectra were histograms consisting of 1000 time bins with a total of around 1 million counts. The 1 million detections collected in 1 s were sufficient for producing a high-fidelity interference spectrum. The acquisition time can be decreased to a fraction of a second if the light intensity is increased in the system and the measurement program is customized to fully use the potential of the FPGA electronics. To acquire a B-scan, the objects were mounted onto a motorized stage (Standa) and laterally translated. The stage could not be translated continuously, because such movement introduced vibrations in the experimental system and led to a drastic drop in the number of detected photons. Discrete scanning was implemented instead, where for every lateral position the physical movement of the stage completely ceases before the spectrum is measured. It extended the single spectrum's acquisition time by an additional 1 s. This technical issue can be solved by mechanically insulating the motorized stage from the rest of the setup.

To assess the performance of the detection system in the context of OCT imaging, a mirror was used as an object, and its axial position was varied to introduce different optical path differences (OPDs) in the interferometer. The axial resolution in air was around 17 μm and dropped from approximately 16.5 μm to 17.9 μm over the distance of 1.1 mm [Fig. 2(d)]. As a reference, a spectrum of the light was measured with an optical spectrum analyzer [Fig. 2(a)]—the FWHM was 65 nm, which at 1550 nm corresponds to a theoretical axial resolution of 16.3 μm (calculated assuming a Gaussian spectrum). The sensitivity was estimated to be 26 dB and was determined based on the signal roll-off [Fig. 2(d)], where the intensity, I, was recalculated to $10 \log(I)$. The same value was obtained when B-scans were considered as described in [11]. The 6 dB falloff was calculated to be at 0.92 mm. The maximum imaging range, i.e., the maximum axial distance at which no aliasing is observed, was 5.1 mm. It means that although the detection system would allow detecting fringes at OPDs up to 5.1 mm, the sensitivity drops so fast that the fringe visibility becomes zero much earlier [compare Figs. 2(b) and 2(c)].

To better understand this depth-dependent sensitivity drop and to see how it can be mitigated, we notice that it is analogous to the signal roll-off observed in traditional spectrometers [10]. The signal roll-off can be used to calculate the sensitivity falloff, which is the decrease of the height of the peak in the A-scan with an increasing OPD. In traditional spectrometers, falloff, F_{gr}, is approximated by the first three terms of Eq. (5) from [10] with the assumptions that the spectrum is distributed on the camera as a linear function of a wavenumber k and that the spectrum itself is Gaussian,

$$F_{gr}(z) = \Delta x R e^{-\frac{a^2 R^2 z^2}{4 \ln 2}} \frac{\sin \Delta x R z}{\Delta x R z}, \tag{1}$$

where Δx is a pixel width of a camera sensor, a is the FWHM of a single-wavelength spot size on the camera, and R is a reciprocal linear dispersion indicating the width of the spectrum that is the

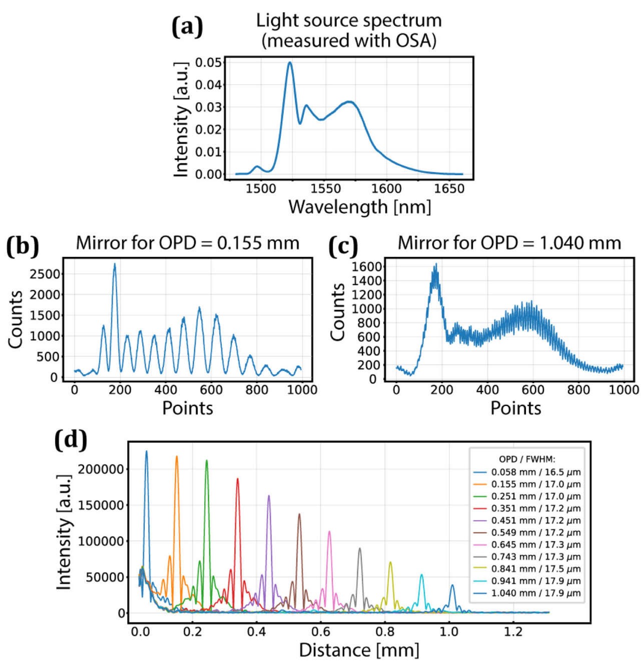

Fig. 2. (a) Spectrum of the pulsed laser measured by an optical spectrum analyzer. (b) and (c) Interference spectra at the optical path difference (OPD) of 0.155 mm and 1.04 mm show the decrease in fringe visibility similar to the one observed for traditional spectrometers [10]. (d) Intensity of the spectra FFT for a mirror as an object for different OPDs of the interferometer. The 6 dB falloff occurs at 0.92 mm, and the axial resolution drops by 1.4 μm—from 16.5 μm to 17.9 μm—on a distance of 1.1 mm.

spectrum in wavenumber spread over 1 μm at the focal plane. The fourth term in Eq. (5) from [10] is omitted here, because it is only responsible for generating Gaussian-shaped peaks in the model and does not contribute to the peaks' height decrease.

The first three terms of Eq. (1) representing a spatial case can be rewritten to a temporal form, F_{temp}, to describe a falloff for fiber-based spectrometers,

$$F_{\mathrm{temp}}(z) = \Delta t R_t e^{-\frac{\delta T^2 R_t^2 z^2}{4 \ln 2}} \frac{\sin \Delta t R_t z}{\Delta t R_t z}, \tag{2}$$

where Δt is the time jitter and replaces the pixel size Δx in Eq. (1). R_t—the temporal analogue of a reciprocal linear dispersion—is the width of the spectrum in wavenumber spread over a time unit at the output of a fiber in fiber-based spectrometers. It is experimentally defined by $R_t = \Delta k / \Delta T$, where Δk is the total width of the spectrum in wavenumber and ΔT is the pulse duration at the output of the long fiber spool. R_t can be rewritten in terms of β_2 and fiber length, L, as $R_t = 1/(c\beta_2 L)$, where c is the speed of light. δT—whose spatial counterpart is the FWHM of a single-wavelength spot size on the camera—is a length of time corresponding to a spectral width equal to the spectral resolution of the fiber's DFT property. It can be calculated using Eq. (21) in [12], $\delta T = 2\sqrt{\pi \beta_2 L}$. z is the OPD in the interferometer.

The formula given in Eq. (2) describes a falloff for linearly sampled spectra, which in DFT can only be achieved when two fiber spools are used [13], because the dispersion of the first fiber is compensated with the dispersion of the other one. To correctly simulate the falloff for a single fiber spool, a more general Eq. (4) from [10] is modified and used,

$$\begin{aligned} I(t_j) = \int_0^\infty \Bigg[&\mathrm{Erf}\left(\frac{(\Delta t - 2t(k) + 2t_j)\sqrt{\ln 2}}{\delta T} \right) \\ &+ \mathrm{Erf}\left(\frac{(\Delta t + 2t(k) - 2t_j)\sqrt{\ln 2}}{\delta T} \right) \Bigg] \\ &[\rho_{\mathrm{ref}}(k) + \rho_{\mathrm{sam}}(k) + 2\sqrt{\rho_{\mathrm{ref}}(k)\rho_{\mathrm{sam}}(k)} \cos \Delta\phi] \mathrm{d}k, \end{aligned} \tag{3}$$

where the spatial spectrum distribution, $x(k)$, is replaced with the temporal spectrum distribution $t(k)$, and the spatial coordinate describing a pixel on the camera sensor, x_j is replaced with temporal coordinate t_j. ρ_{ref} and ρ_{sam} are the reference and sample spectra, and $\Delta\phi$ is the phase difference between the two arms. The signal roll-off was measured and calculated for the lengths $L = 5$ km and 3.5 km of a SMF28E fiber as depicted in Fig. 3. The experimental results are in fairly good agreement with the proposed model.

It has been previously shown that the optimum sensitivity drop in traditional spectrometers is achieved when the ratio of the single-wavelength spot size to the pixel size, $a/\Delta x$, is smaller than 0.25 [14]. When this condition is met, the 6 dB falloff does not occur before the maximum imaging range. The analogue for a fiber spectrometer is $\delta T/\Delta t = 2\sqrt{\pi \beta_2 L}/\Delta t$. Unfortunately, in this case, an optimum does not exist as, unlike for the grating-based spectrometers, the ratio is proportional to the maximum imaging range $1/(R_t \Delta t) = c\beta_2 L/\Delta t$. As they are coupled through the detector and fiber's parameters,

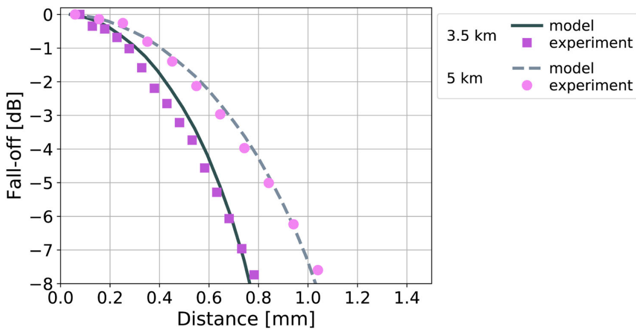

Fig. 3. Theoretical and experimental falloffs calculated for two lengths of a SMF28E fiber: 3.5 km and 5 km. The STD of the jitter, Δt, in the calculations is 35 ps. The temporal equivalent of spectral resolution of the fiber, δT, was calculated to be 32 ps for the 3.5-km-long fiber and 38 ps for the 5-km-long fiber. The falloff, F, was calculated as 10 log(F), where F is normalized.

the 6 dB falloff point and the maximum imaging range move forward simultaneously.

The spectral detection based on a fiber spool and a single-photon detector was used to image two kinds of objects: a stack of glasses (Fig. 4) and an onion (Fig. 5). Each image consists of 450 A-scans and was acquired in 15 min.

The stack of glasses consists of a 50-μm-thick quartz, a 460-μm-thick sapphire, and 500-μm-thick BK7. Because the lateral size of the quartz was substantially smaller than the size of the sapphire, we decided to image the area on the edge of the quartz (Fig. 4). The left-hand side of the images in Fig. 4 corresponds to just the sapphire and the right-hand side corresponds to where the quartz lies on the sapphire. Figure 4(a) presents a raw B-scan obtained after Fourier transforming linearized spectra, and Fig. 4(b) is the same B-scan processed to show the object without artefacts. On both images, one can discern the layer of quartz, an air gap between the quartz and

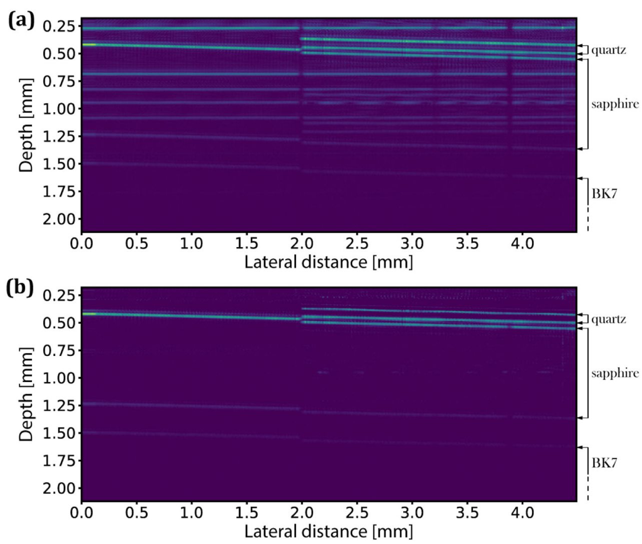

Fig. 4. Image of a stack of glass: quartz (only on the right), air gap, sapphire and an air gap between sapphire and BK7. (a) A B-scan showing an increased sensitivity in detecting interference between photons reflected from every surface of the object. (b) The same B-scan where the additional peaks were removed numerically. Layers way below the 6 dB falloff distance are still visible.

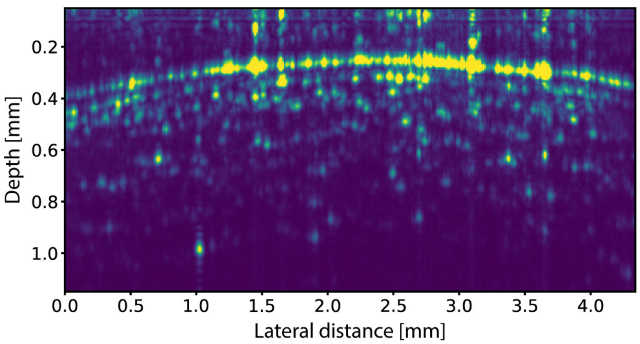

Fig. 5. Image of an onion slice. An average of 10 B-scans acquired at the intensity level of approximately 10 pW.

the sapphire, the layer of sapphire, and an air gap between the sapphire and the BK7. The second air gap is visible at an optical depth of around 1.4 mm despite the 0.92 mm 6 dB sensitivity falloff. However, the high sensitivity of the detection based on single-photon detectors allowed the appearance of "parasitic" peaks, which are associated with the interference of photons backscattered from every two interfaces in the object. Since the location of these self-interference peaks in an A-scan depends on the distance between interfaces, they are not displaced when the OPD is changed and do not disappear when the light from the reference arm is blocked. Consequently, their position will also remain fixed when a laterally scanned stack of glasses is not placed perfectly perpendicular to the direction of light propagation. It results in a B-scan as shown in Fig. 4(a), where the self-interference terms are represented by horizontal lines and the structure by tilted lines. This behavior is used to remove the parasitic peaks by subtracting a mean spectrum from every spectrum in the B-scan file [see Fig. 4(b)]. We should note here that these "parasitic" peaks are always present in the B-scan, irrespective of the angle at which the glasses are positioned with respect to the beam.

The same removal algorithm cannot be used on objects whose structure is more complicated than parallel layers such as biological specimen. A piece of onion (Fig. 5) was imaged to partially visualize the problem. Figure 5 depicts the mean of 10 images at one cross section of the object. The self-interference terms can be seen close to the 0 OPD point. One can discern a cellular structure of the object, but the image is very grainy, even after averaging. Also, the quality of the image can be degraded by the fact that the structure of the object overlaps the area with the self-interference terms. This problem might be remedied if the object is placed at a larger OPD. Nevertheless, the image quality is similar to the quality of images obtained by standard spectral OCT systems with comparable imaging parameters, but orders of magnitude higher input powers [15].

We presented a detection scheme that is widely used for spectral measurements in quantum optics and implemented it for OCT imaging. This detection scheme allows imaging with extremely reduced light intensity levels, around 10 pW, and at the same time, with the same quality as compared to standard OCT systems. Although a 0.9 mm imaging range was reported here, it could in principle be much longer if a longer fiber spool was used and at the same time the repetition rate of the laser decreased, for example with a pulse picker. It should be noted that a longer fiber will cause a higher attenuation and lead to a reduced sensitivity. As an alternative, one can use highly dispersive fibers (dispersion compensation fibers, DCF) or photonic fibers, featuring substantially better trade-off between the dispersion and attenuation. However, those are also significantly more expensive. Moreover, the detection method presented here is not limited to a spectral window centered at 1500 nm. Spectral windows, more relevant for OCT imaging, can be used, down to ones centered around 800 nm. The suitable fiber spools, although more expensive, are available and exhibit higher dispersion. Also, single-photon detectors sensitive in the 800 nm and longer wavelength regions are commercially available. The blessing of a very sensitive detection enabled by single-photon detectors proves to be a curse due to the omnipresent self-interference peaks. Whereas it is very easy to get rid of these peaks for well-defined structures such as glass, these parasitic peaks become problematic for more complicated objects such as biological specimen. In such a case, an efficient artefact removal can possibly be achieved with an algorithm based on deep learning, which has recently proven its superiority in a vast number of problems associated with imaging [16–18].

Funding. Marsden Fund (UoA1509); Dodd-Walls Centre for Photonic and Quantum Technologies (New Ideas); Fundacja na rzecz Nauki Polskiej (First Team).

Disclosures. The authors declare no conflicts of interest.

REFERENCES

1. J. F. De Boer, R. Leitgeb, and M. Wojtkowski, Biomed. Opt. Express **8**, 3248 (2017).
2. P. Hahn, J. Migacz, R. O'Connell, R. S. Maldonado, J. A. Izatt, and C. A. Toth, Ophthalmic Surg. Lasers Imaging Retina **42**, S85 (2011).
3. A. Unterhuber, B. Považay, B. Hermann, H. Sattmann, A. Chavez-Pirson, and W. Drexler, Opt. Express **13**, 3252 (2005).
4. K. Goda and B. Jalali, Nat. Photonics **7**, 102 (2013).
5. S. Moon and D. Y. Kim, Opt. Express **14**, 11575 (2006).
6. K. Goda, A. Fard, O. Malik, G. Fu, A. Quach, and B. Jalali, Opt. Express **20**, 19612 (2012).
7. M. Avenhaus, A. Eckstein, P. J. Mosley, and C. Silberhorn, Opt. Lett. **34**, 2873 (2009).
8. A. Divochiy, M. Misiaszek, Y. Vakhtomin, P. Morozov, K. Smirnov, P. Zolotov, and P. Kolenderski, Opt. Lett. **43**, 6085 (2018).
9. M. Szkulmowski, S. Tamborski, and M. Wojtkowski, Biomed. Opt. Express **7**, 5042 (2016).
10. Z. Hu, Y. Pan, and A. M. Rollins, Appl. Opt. **46**, 8499 (2007).
11. A. Agrawal, T. J. Pfefer, P. D. Woolliams, P. H. Tomlins, and G. Nehmetallah, Biomed. Opt. Express **8**, 902 (2017).
12. K. Goda, D. R. Solli, K. K. Tsia, and B. Jalali, Phys. Rev. A **80**, 043821 (2009).
13. L. Zhang, L. Chen, Z. Lei, Y. Duan, C. Zhang, and X. Zhang, Opt. Lett. **44**, 4135 (2019).
14. Z. Hu and A. M. Rollins, in *Optical Coherence Tomography* (Springer, 2008), pp. 379–404.
15. L. Yu, B. Rao, J. Zhang, J. Su, Q. Wang, S. Guo, and Z. Chen, Opt. Express **15**, 7634 (2007).
16. C. O. da Costa-Luis and A. J. Reader, in *IEEE Nuclear Science Symposium and Medical Imaging Conference (NSS/MIC)* (IEEE, 2017), pp. 1–3.
17. K. J. Halupka, B. J. Antony, M. H. Lee, K. A. Lucy, R. S. Rai, H. Ishikawa, G. Wollstein, J. S. Schuman, and R. Garnavi, Biomed. Opt. Express **9**, 6205 (2018).
18. F. Shi, N. Cai, Y. Gu, D. Hu, Y. Ma, Y. Chen, and X. Chen, Phys. Med. Biol. **64**, 175010 (2019).